The Astrophysical Journal, 761:50 (12pp), 2012 December 10 doi:10.1088/0004-637X/761/1/50

BROADBAND STUDY OF GRB 091127: A SUB-ENERGETIC BURST AT HIGHER REDSHIFT?

E. Troja[1,2,17], T. Sakamoto[1], C. Guidorzi[3,4], J. P. Norris[5], A. Panaitescu[6], S. Kobayashi[4], N. Omodei[7], J. C. Brown[1], D. N. Burrows[8], P. A. Evans[9], N. Gehrels[1], F. E. Marshall[1], N. Mawson[4], A. Melandri[4,10], C. G. Mundell[4], S. R. Oates[11], V. Pal'shin[12], R. D. Preece[13], J. L. Racusin[1], I. A. Steele[4], N. R. Tanvir[9], V. Vasileiou[14], C. Wilson-Hodge[15], and K. Yamaoka[16]

[1] NASA, Goddard Space Flight Center, Greenbelt, MD 20771, USA
[2] Astronomy Department, University of Maryland, College Park, MD 20742, USA
[3] Physics Department, University of Ferrara, via Saragat 1, I-44122, Ferrara, Italy
[4] Astrophysics Research Institute, Liverpool John Moores University, Twelve Quays House, Egerton Wharf, CH41 1LD Birkenhead, UK
[5] Physics Department, Boise State University, 1910 University Drive, Boise, ID 83725, USA
[6] Space Science and Applications, MS D466, Los Alamos National Laboratory, Los Alamos, NM 87545, USA
[7] W. W. Hansen Experimental Physics Laboratory, Kavli Institute for Particle Astrophysics and Cosmology, Department of Physics and SLAC National Accelerator Laboratory, Stanford University, Stanford, CA 94305, USA
[8] Department of Astronomy and Astrophysics, Pennsylvania State University, 525 Davey Lab, University Park, PA 16802, USA
[9] X-ray and Observational Astronomy Group, Department of Physics and Astronomy, University of Leicester, Leicester LE1 7RH, UK
[10] INAF-OAB, via Bianchi 46, I-23807 Merate (LC), Italy
[11] Mullard Space Science Laboratory, University College London, Holmbury St. Mary, Dorking, Surrey RH5 6NT, UK
[12] Ioffe Physico-Technical Institute, Laboratory for Experimental Astrophysics, 26 Polytekhnicheskaya, St Petersburg 194021, Russian Federation
[13] Department of Physics, University of Alabama in Huntsville, NSSTC, 320 Sparkman Drive, Huntsville, AL 35805, USA
[14] Laboratoire Univers et Particules de Montpellier, Université Montpellier 2, and CNRS/IN2P3, F-34095 Montpellier, France
[15] Institute of Astro and Particle Physics, University Innsbruck, Technikerstrasse 25, A-6176 Innsbruck, Austria
[16] Department of Physics and Mathematics, Aoyama Gakuin University, 5-10-1 Fuchinobe, Chuo-ku, Sagamihara, Kanagawa 252-5258, Japan
Received 2012 January 22; accepted 2012 October 6; published 2012 November 21

ABSTRACT

GRB 091127 is a bright gamma-ray burst (GRB) detected by *Swift* at a redshift $z = 0.49$ and associated with SN 2009nz. We present the broadband analysis of the GRB prompt and afterglow emission and study its high-energy properties in the context of the GRB/SN association. While the high luminosity of the prompt emission and standard afterglow behavior are typical of cosmological long GRBs, its low-energy release ($E_\gamma < 3 \times 10^{49}$ erg), soft spectrum, and unusual spectral lag connect this GRB to the class of sub-energetic bursts. We discuss the suppression of high-energy emission in this burst, and investigate whether this behavior could be connected with the sub-energetic nature of the explosion.

Key word: gamma-ray burst: individual (GRB 091127)

Online-only material: color figures

1. INTRODUCTION

It is well established that (most) long-duration gamma-ray bursts (GRBs) are linked to the gravitational collapse of massive stars (Woosley & Bloom 2006). Such a connection is supported by several lines of evidence (Hjorth & Bloom 2011 and references therein). In a few remarkable cases the spectroscopic identification of a broad-line Type Ic SN, co-spatial and coeval with the GRB, provided a direct proof of the physical association between the two phenomena.

With the exception of GRB 030329, whose properties are roughly similar to typical long GRBs (Berger et al. 2003), GRBs with spectroscopically confirmed supernovae (SNe) show a peculiar behavior, both in their prompt and afterglow emission phases (Kaneko et al. 2007; Starling et al. 2011). These bursts are characterized by a relatively softer spectrum ($E_{\rm pk} \lesssim 120$ keV), and a lower energy output ($E_{\gamma,\rm iso} \sim 10^{48}$–$10^{50}$ erg) than standard GRBs. They do not strictly follow the lag–luminosity relation (Norris 2002), whereas they generally agree with the Amati relation (Amati et al. 2007), but with GRB 980425 being a notable outlier. Sub-energetic nearby bursts tend to show a faint afterglow emission, both in X-rays and in the optical band. Late-time radio monitoring of their afterglows showed evidence of a quasi-spherical and only mildly relativistic ($\Gamma \approx 2$) outflow (Soderberg et al. 2006), very different from the highly relativistic and collimated jets observed in long GRBs (Bloom et al. 2003; Molinari et al. 2007; Cenko et al. 2010). For these reasons, it has been speculated that sub-energetic events belong to an intrinsically distinct population of bursts that dominate the local ($z \lesssim 0.5$) rate of observed events (Liang et al. 2007; Chapman et al. 2007).

Whereas the case for spectroscopically confirmed SNe remains confined to nearby GRBs, at higher redshifts ($0.3 < z < 1$) the emergence of the associated SN is pinpointed by a late-time optical rebrightening or "bump" in the afterglow light curves (Bloom et al. 1999; Zeh et al. 2004; Tanvir et al. 2010). Though alternative explanations for such a feature are plausible (Esin & Blandford 2000; Waxman & Draine 2000), a spectroscopic analysis of some of these SN bumps supports their similarity with bright Type Ic SNe (e.g., Della Valle et al. 2006; Sparre et al. 2011). This is the case of GRB 091127, detected by the *Swift* satellite (Gehrels et al. 2004) at a redshift of $z = 0.49$, and associated with SN2009nz. Cobb et al. (2010) identified in the GRB afterglow a late-time optical rebrightening, peaking at a magnitude of $I = 22.3 \pm 0.2$ mag at ~22 days after the burst, and attributed it to the SN light. The photometric properties of SN2009nz resemble SN1998bw (Galama et al. 1998), though displaying a faster temporal evolution and a slightly dimmer

[17] NASA Postdoctoral Program Fellow.

peak magnitude. More recently, the spectroscopic analysis presented by Berger et al. (2011) uncovered the typical undulations of broad-line Type Ic SNe associated with nearby GRBs, thus confirming the SN origin of the photometric bump. Berger et al. (2011) concluded that the explosion properties of SN2009nz ($E_K \approx 2 \times 10^{51}$ erg, $M_{\rm ej} \sim 1.4\ M_\odot$, and $M_{\rm Ni} \approx 0.35\ M_\odot$) are remarkably similar to SN2006aj (Pian et al. 2006), associated with GRB 060218. GRB 091127 therefore represents one of the best cases linking long GRBs and SNe at redshifts $z > 0.3$.

While previous works mainly focused on the properties of SN2009nz and its environment (Cobb et al. 2010; Vergani et al. 2011), in this paper we present a broadband analysis of the GRB prompt and afterglow emission and study the high-energy properties of the explosion in the context of GRB/SN associations. Being a bright and relatively nearby burst, GRB 091127 has a rich multi-wavelength coverage up to very late times, which allows us to study in detail its spectral and temporal evolution (see also Filgas et al. 2011) and compare it to other well-known cases of GRBs/SNe.

The paper is organized as follows. Our observations are detailed in Section 2. In Section 3, we present a multi-wavelength timing and spectral analysis of both the prompt and the afterglow emission. Our results are presented in Section 4 and discussed in Section 5. Finally, in Section 6 we summarize our findings and conclusions. Throughout the paper, times are given relative to the *Swift* trigger time T_0, $t = T - T_0$, and the convention $f_{\nu,t} \propto \nu^{-\beta} t^{-\alpha}$ has been followed, where the energy index β is related to the photon index $\Gamma = \beta + 1$. The phenomenology of the burst is presented in the observer's time frame. Unless otherwise stated, all the quoted errors are given at 90% confidence level for one interesting parameter (Lampton et al. 1976).

2. OBSERVATIONS AND DATA REDUCTION

GRB 091127 triggered the *Swift* Burst Alert Telescope (BAT; Barthelmy et al. 2005) at 23:25:45 UT on 2009 November 27 (Troja et al. 2009). It was also observed by *Konus–Wind*, *Suzaku* Wide-band All-sky Monitor (WAM), and the *Fermi* Gamma-Ray Burst Monitor (GBM). The burst was within the field of view of the *Fermi* Large Area Telescope (LAT; Atwood et al. 2009), at an angle of 25° from the bore sight.

The 2 m Liverpool Telescope (LT) responded robotically to the *Swift* alert and began observing at 23:28:06 UT, 141 s after the BAT trigger. The detection mode of the automatic LT GRB pipeline (Guidorzi et al. 2006) identified a bright optical afterglow ($r' = 15.4$ mag) at $\alpha = 02^{\rm h}26^{\rm m}19\overset{\rm s}{.}89$, $\delta = -18°57'08\overset{''}{.}6$ (J2000) (uncertainty of $0\overset{''}{.}5$; Smith et al. 2009). Observations were obtained with $r'i'z'$ filters until 2.3 hr post-burst. The afterglow was monitored with both the Faulkes Telescope South (FTS) and LT up to six days post-burst within the $BVRr'i'$ filters. Magnitudes of field stars in BVR were calibrated using Landolt standard stars (Landolt 1992) obtained during following photometric nights. Sloan Digital Sky Survey $r'i'z'$ magnitudes of the same field stars were obtained using the transformations by Jordi et al. (2006). Early-time observations were also obtained using SkycamZ, mounted on the LT tube. Observations are filter-less (white light) to maximize the throughput of the optics. The data were dark and bias subtracted in the usual fashion and flat fielded using a stack of twilight exposures. Standard aperture photometry was carried out using two local reference stars, and calibrated by comparison with R-band frames of the same field. Results are reported in Table 3.

Due to an Earth limb constraint, *Swift* did not immediately slew to the burst location and follow-up observations with its two narrow-field instruments, the X-Ray Telescope (XRT; Burrows et al. 2005) and the Ultra-Violet Optical Telescope (UVOT; Roming et al. 2005), began 53 minutes after the trigger. As the X-ray afterglow was still bright ($\sim$10 counts s^{-1}), XRT started collecting data in Windowed Timing (WT) mode, and automatically switched to Photon Counting (PC) mode when the source decreased to $\lesssim$2 counts s^{-1}. Follow-up observations monitored the X-ray afterglow for 36 days for a total net exposure of 760 s in WT mode and 470 ks in PC mode. The optical afterglow was detected by UVOT in the White, v, u, $uvw1$, and $uvm2$ filters at a position consistent with the LT localization. The detection in the UV filters is consistent with the low redshift $z = 0.49$ of this burst. *Swift*/XRT and UVOT data were reduced using the HEASOFT[18] (v6.11) and *Swift* software (v3.8) tools and latest calibration products. We refer the reader to Evans et al. (2007) for further details on the XRT data reduction and analysis. The UVOT photometry was done following the methods described in Breeveld et al. (2010) with adjustments to compensate for the contamination of a nearby star.

In order to monitor the late-time X-ray afterglow, two Target of Opportunity observations were performed by the *Chandra X-Ray Observatory* at $t = 98$ days for a total exposure of 38 ks and $t = 188$ days for a total exposure of 80 ks. *Chandra* data were reduced using version 4.2 of the CIAO software. Source events were extracted from a 2 pixel radius region around the GRB position, while the background was estimated from a source-free area using a 20 pixel radius region.

3. DATA ANALYSIS

3.1. Gamma-ray Data

3.1.1. Temporal Analysis

Figure 1 presents the prompt emission light curves with a 128 ms time resolution and in four different energy bands. The burst duration, defined as the interval containing 90% of the total observed fluence, is T_{90} (15–350 keV) = 7.1 ± 0.2 s. The burst temporal profile is characterized by two main peaks, at $t \sim 0$ s and $t \sim 1.1$ s, respectively. They are clearly detected up to ~600 keV and display a soft-to-hard spectral evolution. A period of faint, spectrally soft emission lasting ~8 s, follows. On top of it a third peak at $t \sim 7$ s is visible at energies below 50 keV.

Spectral lags were calculated by cross-correlating the light curves in the standard BAT channels: 1 (15–25 keV), 2 (25–50 keV), 3 (50–100 keV), 4 (100–350 keV). In order to increase the signal to noise in the higher energy channels, the analysis was performed on non mask-weighted light curves, each with a 8 ms time resolution. We derived $\tau_{31} = 2.2^{+22.8}_{-11.3}$ ms and $\tau_{42} = -9.2^{+8.2}_{-6.5}$ ms, where the quoted uncertainties (at a 1σ confidence level) were evaluated by simulations. Lag analysis reveals a significant difference between the two main γ-ray peaks (a and b in Figure 1). The former shows positive lags, $\tau_{31} = 36^{+24}_{-16}$ ms and $\tau_{42} = 16^{+13}_{-13}$ ms, while the latter has negligible or negative lags, $\tau_{31} = -2^{+12}_{-12}$ ms and $\tau_{42} = -14^{+7}_{-3}$ ms.

3.1.2. Search for High-energy γ-Ray Emission

The *Fermi*/LAT data were searched for emission during the prompt γ-ray phase and over longer timescales (up to 10 ks). The

[18] http://heasarc.gsfc.nasa.gov/docs/software/lheasoft/

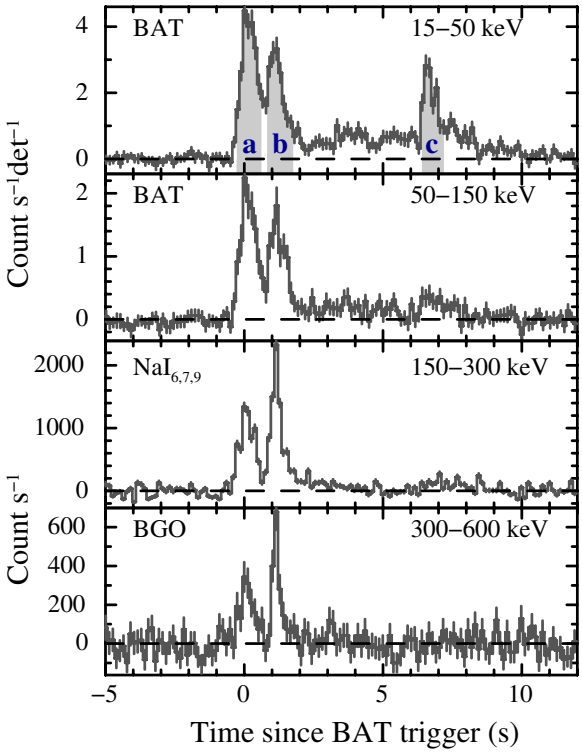

Figure 1. *Swift*/BAT (top two panels) and *Fermi*/GBM (bottom two panels) background-subtracted light curves of GRB 091127 with a 128 ms binning. The gray areas labeled as *a*, *b*, and *c* in the top panel show the three intervals selected for the time-resolved spectral analysis. Error bars are 1σ.

searches were performed by means of an unbinned likelihood analysis (Abdo et al. 2009). We used the Pass7V6 Transient class events with a reconstructed energy above 100 MeV. We selected events within 12° around the best burst position (see Section 2), and applied a cut on zenith angle at 105° in order to limit the contamination from the bright Earth's limb. For the Transient data class, the dominant background component is the isotropic background due to residual charged particles misclassified as γ-rays. We modeled it by using the tool developed by the LAT collaboration that can estimate the hadronic cosmic-ray and γ-ray components of the background with an accuracy of ≈10%–15% (Abdo et al. 2009). We also added the template `gal_2yearp7v6_v0.fits`[19] describing the Galactic diffuse emission due to the interaction of cosmic rays with the gas and the interstellar radiation field.

No significant excess above background was found. Following the procedure described in Abdo et al. (2009) and by fixing the photon index to 2.25, we derived a 95% upper limit of 2.8×10^{-8} erg cm^{-2} s^{-1} in the 100 MeV–1 GeV energy range and of 1.6×10^{-8} erg cm^{-2} s^{-1} in the 1–10 GeV energy range during the prompt emission interval (-0.3 s $< t <$ 8.2 s).

3.1.3. Spectral Analysis

We performed a time-averaged and a time-resolved spectral analysis, selecting the time intervals in correspondence of the three main pulses as shown in Figure 1 (top panel). The spectral fits were performed in the 15–150 keV energy band for BAT, 20 keV–10 MeV for *Konus–Wind*, and 120 keV–3 MeV for *Suzaku*-WAM, and 100 MeV–10 GeV for LAT. Following Sakamoto et al. (2011), we added a 5% systematic error in the WAM spectra below 400 keV. The intercalibration between BAT, *Konus–Wind,* and *Suzaku*-WAM was extensively studied by Sakamoto et al. (2011), showing an overall agreement in the effective area correction (<20%) between the three instruments. GBM data were fit in the 8–860 keV band for the NaI detectors, and in the 200 keV–40 MeV for the BGO detector. Given the brightness of this burst, we added a 5% systematic error to the GBM data. A cross-calibration study has not been performed with the *Fermi* data yet. Previous works (e.g., Page et al. 2009) report a typical effective area correction factor of ∼1.23 compared to a value of unity for BAT, and in our analysis we found consistent values.

The best-fit spectral parameters were estimated using the maximum likelihood method and, when necessary, by applying different statistics to the data. BAT mask-weighted spectra have Gaussian-distributed uncertainties, and they require the χ^2 statistics to be applied. LAT spectra are instead characterized by low counts, and they can only be modeled using the Poisson distribution. In order to properly account for the Poissonian nature of the source counts and for the Gaussian uncertainties associated to the LAT background model (Abdo et al. 2009), we used the profile likelihood statistic as implemented in the option PGSTAT of XSPEC (Arnaud et al. 2011). Table 1 reports the spectral fit results for the time-averaged analysis. Different spectral models, usually adopted to describe the GRB prompt emission spectrum, were fit to the data: a power law, a power-law with a high-energy cutoff (CPL; $F(E) \propto E^{\alpha}e^{-E/E_{\rm cut}}$), a Band model (Band et al. 1993), and a Band model with a high-energy cutoff (Band+Cut). We also included the log-parabolic function (LOGP; $F(E) \propto E^{\alpha+\beta\log E}$) suggested by Massaro et al. (2010). The last column of Table 1 reports the fit statistics (STAT) and degrees of freedom (dof) for each model. In general, STAT $= \chi^2$, when LAT data were included in the fit STAT $= \chi^2$+PGSTAT.

Additional models, not reported in Table 1, were tested. A single-temperature blackbody plus a power-law yields a poor fit (STAT/dof = 905/574), the addition of a high-energy cutoff significantly improves the fit (STAT/dof = 675/573), but the model is not statistically preferred to the standard Band function with a high-energy cutoff (STAT/dof = 652/573). A multicolor blackbody (Ryde et al. 2010) gives similar results. According to our fit, the burst total fluence is $(1.9 \pm 0.3)\times10^{-5}$ erg cm^{-2} (Band model; see also Nava et al. 2012), and $(1.6 \pm 0.3)\times10^{-5}$ erg cm^{-2} (Band+Cut) in the 8–1000 keV energy band.

Table 2 reports the results of the time-resolved spectral analysis for both intervals *a* and *b*. As found for the time-integrated spectrum, alternative models do not provide an improvement in the fit statistics and are not reported in the table.

The spectrum of the third peak (interval *c* in Figure 1) is well described by a power-law of photon index $\Gamma_{\rm BAT} = 2.78 \pm 0.18$. The average observed flux during this interval is $8^{+1.1}_{-2.0} \times 10^{-7}$ erg cm^{-2} s^{-1}in the 15–50 keV band.

3.2. X-Ray Data

The XRT light curve is well described (χ^2/dof = 376/364) by a power-law decay with slope $\alpha_1 = 1.03 \pm 0.04$ steepening to $\alpha_2 = 1.55 \pm 0.03$ at $t_{\rm bk} = 32^{+9}_{-6}$ ks. The two *Chandra* detections lie slightly above the extrapolation of this model, but are consistent with it within 3 σ. This constrains the time of any late-time jet-break in the X-ray light curve to $t \gtrsim 115$ days. This time was determined by forcing in the fit an additional

[19] Available at the Fermi Science Support Center Web site http://fermi.gsfc.nasa.gov/ssc/data/access/lat/BackgroundModels.html.

Table 1
Spectral Fit Results of the Time-averaged Analysis

Detector	Model	$-\alpha$	$-\beta$	$E_{\rm pk}$ (keV)	$E_{\rm cut}$ (keV)	STAT/dof
BAT	PL	2.17 ± 0.07	...	...	...	52/57 (0.91)
KW	PL	2.19 ± 0.04	...	...	...	74/59 (1.26)
KW	CPL	2.00 ± 0.10	...	...	510^{+440}_{-180}	57/58 (0.98)
WAM	PL	$2.35^{+0.17}_{-0.19}$	...	...	...	23/25 (0.90)
WAM	CPL	1.9 ± 0.5	...	...	>400	20/24 (0.85)
GBM	LOGP	0.73 ± 0.14	0.37 ± 0.04	...	...	465/396 (1.18)
GBM	Band	1.20 ± 0.16	2.23 ± 0.04	39 ± 5	...	457/395 (1.16)
GBM	Band+Cut	$0.3^{+0.9}_{-1.3}$	1.94 ± 0.08	25^{+16}_{-5}	500^{+300}_{-130}	448/394 (1.14)
GBM+LAT	LOGP	0.73 ± 0.14	0.37 ± 0.04	...	...	468/398 (1.18)
GBM+LAT	Band	1.34 ± 0.16	2.32 ± 0.06	45 ± 5	...	485/397 (1.21)
GBM+LAT	Band+Cut	$0.6^{+0.7}_{-1.5}$	$1.96^{+0.19}_{-0.08}$	26^{+15}_{-7}	530^{+400}_{-160}	450/396 (1.14)
JOINT	LOGP	$0.81^{+0.13}_{-0.10}$	0.35 ± 0.04	...	...	632/544 (1.16)
JOINT	Band	1.37 ± 0.12	2.31 ± 0.05	45 ± 4	...	640/543 (1.18)
JOINT	Band+Cut	$1.06^{+0.2}_{-1.18}$	$2.07^{+0.12}_{-0.08}$	36^{+6}_{-12}	800^{+800}_{-300}	602/542 (1.11)

Table 2
Spectral Fit Results of the Time-resolved Analysis

Detector	Model	$-\alpha$	$-\beta$	$E_{\rm pk}$ (keV)	$E_{\rm cut}$ (keV)	STAT/dof
Time interval *a*: from $T_0 - 0.3$ s to $T_0 + 0.7$ s						
BAT	PL	1.91 ± 0.10	...	...	...	59/57 (1.03)
WAM	PL	$2.42^{+0.10}_{-0.12}$	...	...	...	39/34 (1.15)
WAM	CPL	1.89 ± 0.5	...	...	600^{+2000}_{-300}	33/33 (1.00)
GBM	LOGP	<0.017	0.54 ± 0.02	...	...	313/270 (1.16)
GBM	Band	0.54 ± 0.16	2.27 ± 0.07	56 ± 5	...	257/269 (0.95)
GBM	Band+Cut	$0.4^{+0.18}_{-0.2}$	1.97 ± 0.17	54 ± 6	600^{+900}_{-200}	247/268 (0.92)
GBM+LAT	LOGP	<0.019	0.55 ± 0.02	...	...	314/272 (1.15)
GBM+LAT	Band	0.60 ± 0.15	2.32 ± 0.06	59 ± 5	...	266/271 (0.98)
GBM+LAT	Band+Cut	$0.4^{+0.18}_{-0.2}$	1.97 ± 0.17	54 ± 6	600^{+900}_{-200}	248/270 (0.92)
JOINT	LOGP	<0.021	0.54 ± 0.02	...	...	413/365 (1.13)
JOINT	Band	0.63 ± 0.13	2.34 ± 0.06	59 ± 5	...	369/364 (1.01)
JOINT	Band+Cut	$0.41^{+0.18}_{-0.2}$	2.02 ± 0.11	53 ± 5	700^{+600}_{-300}	344/363 (0.95)
Time interval *b*: from $T_0 + 0.8$ s to $T_0 + 1.7$ s						
BAT	PL	1.78 ± 0.12	...	...	...	52/57 (0.92)
WAM	PL	2.38 ± 0.11	...	...	...	34/34 (1.00)
WAM	CPL	$1.8^{+0.4}_{-0.5}$	...	...	1000^{+4000}_{-600}	28/33 (0.87)
GBM	LOGP	0.35 ± 0.16	0.38 ± 0.05	...	...	263/270 (0.97)
GBM	Band	$1.22^{+0.08}_{-0.12}$	$2.23^{+0.2}_{-0.13}$	140 ± 30	...	257/269 (0.95)
GBM	Band+Cut	$1.22^{+0.10}_{-0.13}$	$2.13^{+0.2}_{-0.13}$	140 ± 30	>900	257/268 (0.96)
GBM+LAT	LOGP	0.33 ± 0.15	0.37 ± 0.05	...	...	263/272 (0.97)
GBM+LAT	Band	1.31 ± 0.06	$2.6^{+0.8}_{-0.3}$	170 ± 30	...	256/271 (0.94)
GBM+LAT	Band+Cut	1.30 ± 0.07	2.52 ± 0.17	170 ± 30	>700	252/270 (0.93)
JOINT	LOGP	$0.29^{+0.16}_{-0.13}$	0.38 ± 0.04	...	...	366/364 (1.00)
JOINT	Band	1.32 ± 0.06	$2.51^{+0.16}_{-0.27}$	170^{+30}_{-20}	...	361/363 (0.99)
JOINT	Band+Cut	$1.29^{+0.08}_{-0.10}$	2.34 ± 0.12	160^{+50}_{-20}	>1000	356/362 (0.98)

break with $\Delta\alpha = 1$, and by varying the break time until a $\Delta\chi^2 = 2.706$ was reached.

During our observations a slight soft-to-hard spectral evolution is visible over the first few hours. We performed time-resolved spectral fits on seven consecutive time intervals, selected according to the light curve phases and to have ~1000 net counts each. The X-ray spectra were modeled with an absorbed power-law. We derived an intrinsic $N_{\rm H} = 9^{+4}_{-3} \times 10^{20}$ cm^{-2} at $z = 0.49$, in excess of the Galactic value of 2.8×10^{20} cm^{-2} (Kalberla et al. 2005). The resulting photon indices Γ_X, ranging from 2.02 ± 0.10 to 1.82 ± 0.09, are consistent within the uncertainties, however a systematic trend of a slowly decreasing Γ_X is evident. The time-averaged photon index is $\Gamma_X = 1.88 \pm 0.08$.

Because of the low number of events in the *Chandra* spectrum (67 net counts) we used the Cash statistics (Cash 1979) and fit it with an absorbed power-law by fixing the absorption components to the values quoted above. The resulting photon index is $\Gamma_X = 1.6 \pm 0.3$, from which we calculate an energy conversion factor of $\sim 1.1 \times 10^{-11}$ erg cm^{-2} count^{-1}.

3.3. Optical Data

The optical afterglow light curves, including data from UVOT, LT, FTS, and SkycamZ, and the X-ray afterglow light curve, reporting the XRT (filled circles) and *Chandra* (open circles) data, are shown in Figure 2. The best-fit models are also shown (optical: dashed lines; X-ray: solid line).

Table 3
Photometric Data Set for the Afterglow of GRB091127

Time[a] (s)	Facility	Exposure (s)	Filter	Magnitude[b]	Time[a] (s)	Facility	Exposure (s)	Filter	Magnitude[b]
146.0	LT	10	r'	15.41 ± 0.02	153.0	Skycam	10	C	15.09 ± 0.08
168.2	LT	10	r'	15.45 ± 0.02	212.0	Skycam	10	C	15.23 ± 0.09
191.0	LT	10	r'	15.58 ± 0.02	274.0	Skycam	10	C	15.49 ± 0.11
422.0	LT	10	r'	15.95 ± 0.03	333.0	Skycam	10	C	15.80 ± 0.14
444.8	LT	10	r'	16.02 ± 0.03	393.0	Skycam	10	C	15.62 ± 0.12
468.8	LT	10	r'	16.00 ± 0.03	453.0	Skycam	10	C	15.75 ± 0.13
760.2	LT	120	r'	16.16 ± 0.01	513.0	Skycam	10	C	15.88 ± 0.14
1413.0	LT	120	r'	16.32 ± 0.01	573.0	Skycam	10	C	16.00 ± 0.16
1546.2	LT	120	r'	16.34 ± 0.01	664.0	Skycam	10	C	15.82 ± 0.10
2662.8	LT	120	r'	16.52 ± 0.01	783.5	Skycam	10	C	16.08 ± 0.13
2794.8	LT	120	r'	16.53 ± 0.02	903.5	Skycam	10	C	16.04 ± 0.11
2926.8	LT	120	r'	16.55 ± 0.02	1023.0	Skycam	10	C	15.89 ± 0.10
4878.2	LT	10	r'	16.74 ± 0.05	1144.0	Skycam	10	C	15.92 ± 0.11
4899.8	LT	10	r'	16.71 ± 0.05	1265.0	Skycam	10	C	16.14 ± 0.13
4922.0	LT	10	r'	16.72 ± 0.05	1382.5	Skycam	10	C	16.09 ± 0.12
5157.8	LT	10	r'	16.76 ± 0.05	1504.0	Skycam	10	C	15.93 ± 0.10
5180.0	LT	10	r'	16.82 ± 0.06	1623.0	Skycam	10	C	16.27 ± 0.14
5204.0	LT	10	r'	16.77 ± 0.06	1743.5	Skycam	10	C	15.96 ± 0.10
5494.8	LT	120	r'	16.83 ± 0.03	48385.2	FTS	300	B	18.78 ± 0.07
6139.2	LT	120	r'	16.88 ± 0.03	48708.0	FTS	300	B	18.82 ± 0.08
6271.8	LT	120	r'	16.91 ± 0.03	49029.0	FTS	300	B	18.71 ± 0.09
7390.2	LT	120	r'	17.00 ± 0.03	49351.2	FTS	300	B	18.84 ± 0.07
7521.0	LT	120	r'	16.99 ± 0.03	55294.2	FTS	300	B	19.03 ± 0.07
7654.2	LT	120	r'	16.99 ± 0.03	55615.8	FTS	300	B	18.94 ± 0.08
77200.2	LT	300	r'	19.25 ± 0.03	55936.8	FTS	300	B	19.06 ± 0.08
77512.2	LT	300	r'	19.27 ± 0.03	56259.0	FTS	300	B	18.98 ± 0.08
77824.2	LT	300	r'	19.29 ± 0.03	40923.0	FTS	300	V	18.37 ± 0.05
78138.0	LT	300	r'	19.30 ± 0.03	41244.0	FTS	300	V	18.46 ± 0.10
78448.8	LT	300	r'	19.27 ± 0.03	41566.2	FTS	300	V	18.38 ± 0.05
78760.8	LT	300	r'	19.34 ± 0.04	41887.2	FTS	300	V	18.36 ± 0.05
88690.2	LT	300	r'	19.50 ± 0.04	49773.0	FTS	300	V	18.60 ± 0.05
89002.2	LT	300	r'	19.44 ± 0.05	50094.0	FTS	300	V	18.61 ± 0.05
89314.2	LT	300	r'	19.45 ± 0.04	50416.2	FTS	300	V	18.63 ± 0.06
89628.0	LT	300	r'	19.53 ± 0.08	50737.8	FTS	300	V	18.64 ± 0.06
162917.0	LT	1800	r'	20.44 ± 0.08	56647.8	FTS	300	V	18.82 ± 0.06
509520.0	LT	1800	r'	>20.8	56968.8	FTS	300	V	18.83 ± 0.06
979.8	LT	120	i'	16.17 ± 0.03	57291.0	FTS	300	V	18.80 ± 0.06
1831.2	LT	120	i'	16.35 ± 0.03	57612.0	FTS	300	V	18.80 ± 0.06
1963.8	LT	120	i'	16.37 ± 0.03	47032.2	FTS	300	R	18.51 ± 0.08
3277.2	LT	120	i'	16.54 ± 0.03	47353.8	FTS	300	R	18.30 ± 0.06
3409.2	LT	120	i'	16.54 ± 0.03	47676.0	FTS	300	R	18.37 ± 0.06
3541.2	LT	120	i'	16.57 ± 0.03	47998.2	FTS	300	R	18.45 ± 0.07
5707.8	LT	120	i'	16.78 ± 0.03	53940.0	FTS	300	R	18.56 ± 0.04
6553.8	LT	120	i'	16.85 ± 0.03	54262.2	FTS	300	R	18.64 ± 0.04
6685.8	LT	120	i'	16.86 ± 0.03	54583.8	FTS	300	R	18.60 ± 0.04
8004.0	LT	120	i'	16.98 ± 0.03	54906.0	FTS	300	R	18.65 ± 0.04
8136.0	LT	120	i'	17.00 ± 0.03	301208.1	FTS	900	R	21.16 ± 0.15
8268.0	LT	120	i'	17.01 ± 0.03	42283.8	FTS	300	i'	18.34 ± 0.05
75250.8	LT	300	i'	19.09 ± 0.05	42606.0	FTS	300	i'	18.37 ± 0.05
75562.2	LT	300	i'	19.12 ± 0.05	42928.2	FTS	300	i'	18.34 ± 0.05
75877.2	LT	300	i'	19.08 ± 0.05	43249.2	FTS	300	i'	18.46 ± 0.06
76189.2	LT	300	i'	19.12 ± 0.05	43570.8	FTS	300	i'	18.39 ± 0.06
76501.2	LT	300	i'	19.05 ± 0.05	51415.2	FTS	300	i'	18.59 ± 0.05
76813.2	LT	300	i'	19.11 ± 0.05	51736.8	FTS	300	i'	18.59 ± 0.05
165408.	LT	1800	i'	20.41 ± 0.08	52057.8	FTS	300	i'	18.59 ± 0.05
336499.	LT	1800	i'	21.25 ± 0.15	52380.0	FTS	300	i'	18.64 ± 0.05
511463.	LT	1800	i'	>20.0	52702.2	FTS	300	i'	18.61 ± 0.05
1200.0	LT	120	z'	16.25 ± 0.05	58005.0	FTS	300	i'	18.77 ± 0.05
2242.8	LT	120	z'	16.43 ± 0.05	58327.2	FTS	300	i'	18.76 ± 0.05
2374.8	LT	120	z'	16.41 ± 0.05	58648.8	FTS	300	i'	18.76 ± 0.05
5925.0	LT	120	z'	16.84 ± 0.07					
6976.2	LT	120	z'	16.87 ± 0.07					
7108.2	LT	120	z'	16.91 ± 0.07					

Notes.
[a] Midpoint time from the GRB trigger.
[b] Errors are $1\,\sigma$.

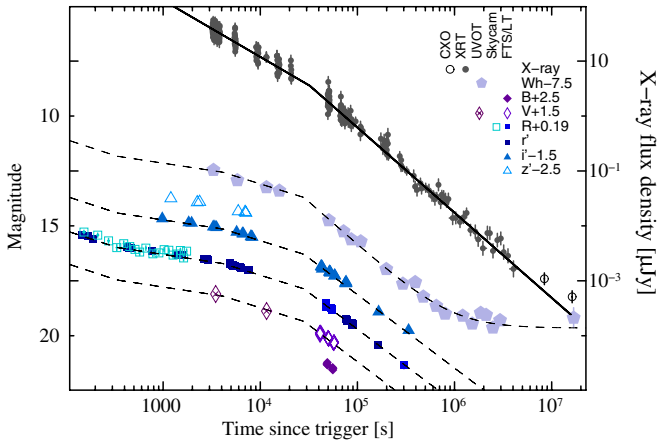

Figure 2. X-ray and optical afterglow light curves of GRB 091127 with the best-fit models overplotted (solid and dashed lines, respectively). At late times ($t > 10$ days), the optical emission is dominated by the underlying host galaxy. Error bars are 1σ. Optical magnitudes are not corrected for Galactic extinction.

(A color version of this figure is available in the online journal.)

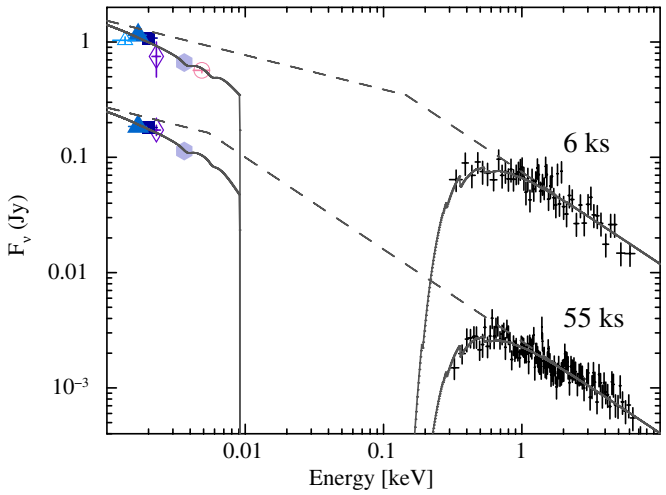

Figure 3. Afterglow spectral energy distributions at 6 ks and 55 ks. The best-fit model (solid line) and the same model corrected for extinction and absorption effects (dashed line) are shown.

(A color version of this figure is available in the online journal.)

The UVOT/White light curve is well described by a broken power-law plus a constant that accounts for the host galaxy emission. The afterglow initially decays with a slope of 0.56 ± 0.04, steepening to 1.57 ± 0.05 after ~29 ks. We estimate a host galaxy contribution of 23.4 ± 0.15 mag.

A significant afterglow color evolution ($\Delta_{I-B} \sim 0.25$ mag) over the course of the first night was reported by Haislip et al. (2009). In the fit of the multicolor light curves we initially allowed for frequency-dependent slopes and/or temporal breaks, but the sparse sampling in the B, V, and z' filters does not allow us to detect any color variation. As we found consistent results between the different filters, we performed a joint fit of the $BVRr'i'z'$ light curves by leaving the normalizations free to vary and tying the other model parameters. The best-fit model requires three temporal breaks ($\chi^2/\mathrm{dof} = 53/70$). The model parameters are: $\alpha_1 = 0.58 \pm 0.12$, $t_{\mathrm{bk},1} = 330^{+190}_{-70}$ s, $\alpha_2 = 0.27 \pm 0.01$, $t_{\mathrm{bk},2} = 4.1^{+0.7}_{-2}$ ks, $\alpha_3 = 0.55 \pm 0.10$, $t_{\mathrm{bk},3} = 28^{+6}_{-5}$ ks, $\alpha_4 = 1.34 \pm 0.04$. Contamination from the SN-bump and the host galaxy light, not detected in the early-time LT exposures, may explain the shallower temporal index at late times. By including in the fit a constant component with magnitude $I = 2\ 2.54 \pm 0.10$ to account for the host emission and a SN-like bump, based on the observation of Cobb et al. (2010), the afterglow slope steepens to $\alpha_4 = 1.64 \pm 0.06$.

3.4. Spectral Energy Distribution

An optical-to-X-ray spectral energy distribution (SED) was produced at two different times, 6 ks and 55 ks, selected because of the good color information and in order to study the spectral evolution across the achromatic temporal break at ~30 ks. Two X-ray spectra were produced, the former in the pre-break interval 9–20 ks, the latter in the post-break interval 50–1000 ks, and scaled to match the observed count rate at each time of interest. The two SEDs were jointly fit in count space (Starling et al. 2007) either with a power-law or a broken power-law continuum. In the latter case, the two spectral slopes were tied to obey the standard afterglow closure relations. Two dust and gas components, modeling the Galactic and intrinsic host extinction and absorption, were also included in the fit. We assumed a solar metallicity for the absorption components and constrained them to the values derived from the XRT spectral fits. We tested three canonical laws—Milky Way (MW), Small Magellanic Cloud (SMC), and Large Magellanic Cloud (LMC)—for the host galaxy extinction by using the parameterization of Pei (1992).

The resulting fit is shown in Figure 3. Both SEDs are well described ($\chi^2 = 146$ for 168 dof) by a broken power-law with indices $\beta_1 = 0.300^{+0.05}_{-0.010}$, $\beta_2 = \beta_1 + 0.5 = 0.800^{+0.05}_{-0.010}$ and a decreasing break energy of $E_{\mathrm{bk}} = 0.15 \pm 0.03$ keV at 6 ks and $E_{\mathrm{bk}} = 6^{+7}_{-4}$ eV at 55 ks. An LMC-type extinction with $E(B-V) = 0.036 \pm 0.015$ mag is only slightly preferred ($\Delta\chi^2 < 2$) to an MW-type or an SMC-type law.

4. RESULTS

4.1. Prompt Emission Properties

4.1.1. Spectral Lags

A common property of long GRBs is that soft energy photons are delayed with respect to the higher energy ones. The measurement of such lags is a valuable tool in the study of GRBs and their classification (e.g., Gehrels et al. 2006). Systematic studies of *BATSE* and *Swift* bursts show that long GRBs predominantly have large, positive lags, ranging from 25 ms to ~200 s (Norris 2002; Norris et al. 2005; Ukwatta et al. 2010), while negligible lags are characteristic of short-duration bursts (Norris & Bonnell 2006; Gehrels et al. 2006) and high-luminosity long GRBs (Norris 2002).

The prompt emission of GRB 091127 seems to not fit in this classification scheme. We measured a small spectral lag of $\tau_{31} \sim 2.2$ ms, consistent with zero, in the BAT channels 3–1, and a negative lag of $\tau_{42} \sim -9.2$ ms in the BAT channels 4–2. The burst position in the lag–luminosity plane is shown in Figure 4, where we also report data for short and long GRBs from the literature (Gehrels et al. 2006; McBreen et al. 2008). Having a negligible lag and only a moderate isotropic peak luminosity ($L_{\mathrm{pk,iso}} \sim 5 \times 10^{51}$ erg s^{-1}), GRB 091127 does not follow the trend of cosmological long GRBs, analogously to underluminous bursts such as GRB 980425. Nearby sub-energetic bursts (with or without an associated SN) are outliers of the lag–luminosity relation (thick dashed line). The inclusion of GRB 091127 suggests that instead of simply being outliers,

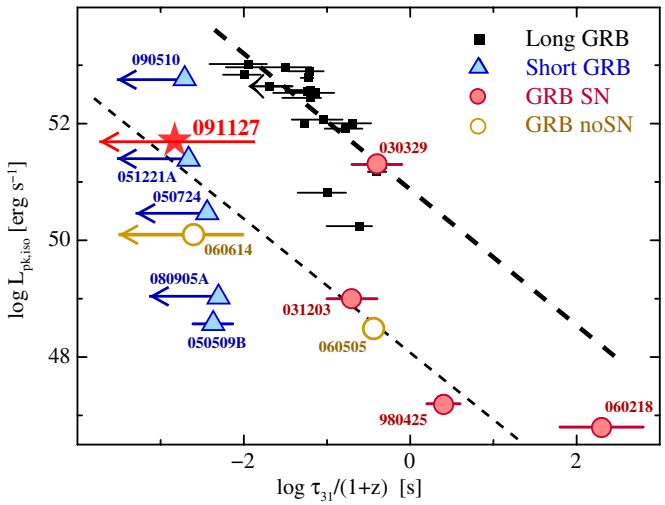

Figure 4. Lag–luminosity diagram for long GRBs (squares), short GRBs (triangles), nearby GRBs with SNe (filled circles) and without SN (open circles). Error bars are 1σ.

(A color version of this figure is available in the online journal.)

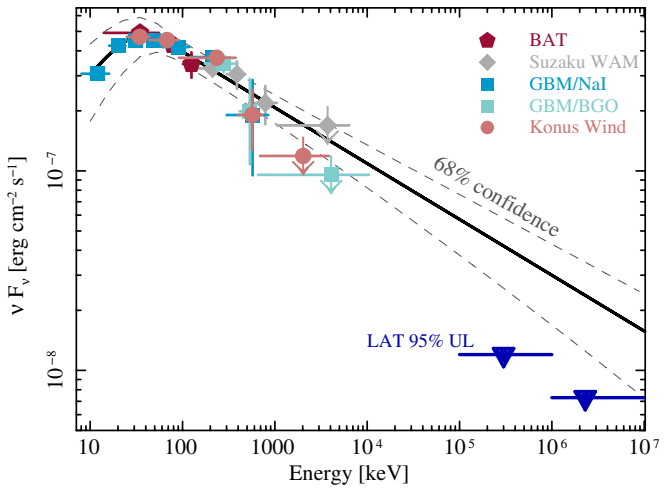

Figure 5. Best-fit Band model of the time-averaged spectrum (solid line) with its 1σ confidence interval (dashed lines). Data from *Swift*/BAT, *Suzaku*-WAM, GBM, and Konus–*Wind* are reported with their 1σ error bars. Upper limits from *Fermi*/LAT are also shown.

(A color version of this figure is available in the online journal.)

there might be a population of bursts following a distinct trend (thin dashed line). While a larger sample of nearby bursts is needed to test this hypothesis, an immediate result coming from Figure 4 is that GRB 091127, which is securely associated with a massive star progenitor, intercepts the bright end of the short GRB population, showing that the scatter of long GRBs in the lag–luminosity plane is larger than previously thought.

In the case of GRB 091127, thanks to the GRB low redshift and low intrinsic extinction, the associated SN was easily revealed by ground-based follow-up observations (Cobb et al. 2010; Berger et al. 2011), nailing down the nature of the GRB progenitor. However, had the same GRB occurred at a higher redshift, its classification would mostly rely on its high-energy properties. At $z > 3$ the faint soft emission would be under the BAT detection threshold, and the GRB would appear as a zero lag, intrinsically short ($T_{90}/(1+z) \lesssim 2$ s) burst, similar to GRB 080913 and GRB 090423 for which a merger-type progenitor was also considered (e.g., Zhang et al. 2009). It is also possible that some of the higher redshift short-duration bursts arise from massive star collapses (e.g., Virgili et al. 2011).

4.1.2. Softening of the High-energy Spectrum

Fitting results are listed in Table 1 for the time-averaged spectrum and in Table 2 for the time-resolved analysis. By describing the time-integrated spectrum with the canonical Band function we obtained typical parameters: $\alpha \sim -1.3$, $\beta \sim -2.3$, and a soft peak energy of ∼45 keV. However, by extrapolating the best-fit Band model to the LAT energy range, the predicted flux in the 100 MeV–1 GeV energy band is $\approx 10^{-7}$ erg cm^{-2} s^{-1}, well above the 95% upper limit derived in Section 3.1.2. This is shown in Figure 5, where we report the observed data with their best-fit Band model extrapolated to the LAT energy range.

The joint fits reported in Table 1 confirm that *Fermi*/LAT observations are not consistent with the extension of a Band function from low to high energies, but require a steepening of the spectrum at energies below 100 MeV. The inclusion of a high-energy spectral break, which we modeled as an exponential cutoff, improves the fit ($\Delta - \mathrm{STAT} = 38$ for one additional degree of freedom). Such a break is particularly evident in the *Konus–Wind* and in the GBM spectra, and we note that the two fits yield consistent values of the cutoff energy and an improvement in the fit statistic of $\Delta\chi^2 = 14$ and $\Delta\chi^2 = 9$, respectively. The quality of the data does not allow us to constrain the spectral index above the break energy and distinguish between a steepening of the power-law decay or an exponential cutoff. By modeling the high-energy data with a simple power-law we derive a photon index of ~ -3.6, and set an upper limit < -2.6 (90% confidence level). The significance of the high-energy break was tested by simulating 10,000 spectra with a simple Band shape. We jointly fit each set of spectra with a Band function (our null model) and a Band function with an exponential cutoff (the alternative model). The fractional number of simulations in which $\Delta - \mathrm{STAT} \geqslant 38$ gives the chance probability that a high-energy spectral break improves the fit. None of the simulations showed a variation of the statistics as high as the one observed, confirming that the presence of a spectral break is statistically preferred at a >99.99% level.

The log-parabolic model of Massaro et al. (2010) also provides a better fit than the standard Band function (STAT/dof = 679/575 versus 690/574), and naturally accounts for the observed suppression of the high-energy emission.

A time-resolved spectral analysis temporally localizes the spectral break during the first γ-ray peak (interval *a*). In this case, the presence of a cutoff at energies ≈500–1000 keV decreases the fit statistics of $\Delta - \mathrm{STAT} = 25$. The lower significance with respect to the time-averaged analysis is likely due to the lack of *Konus–Wind* data in this fit, however, the observed break is evident in both the WAM and in the GBM spectra at a folding energy $E_{\rm cut}$ consistent between the different instruments. According to this model, the observed fluence during the first peak is $(4.3 \pm 0.6) \times 10^{-6}$ erg cm^{-2} in the 8–1000 keV energy band. At a redshift $z = 0.49$ this corresponds to an isotropic equivalent energy $E_{\gamma,\rm iso} = (3.5 \pm 0.5) \times 10^{51}$ erg in the 1–10,000 keV rest-frame energy band. In this time interval the derived value of the low-energy index is $\alpha = -0.41^{+0.18}_{-0.2}$, which is harder but marginally consistent with the limit of 2/3 imposed by the optically thin synchrotron emission. The presence of a thermal component is sometimes invoked to explain the hardest low-energy spectral indices (e.g., Ghirlanda et al. 2003). As already noted in Section 3.1, we tested this hypothesis and found that in no case does the inclusion of

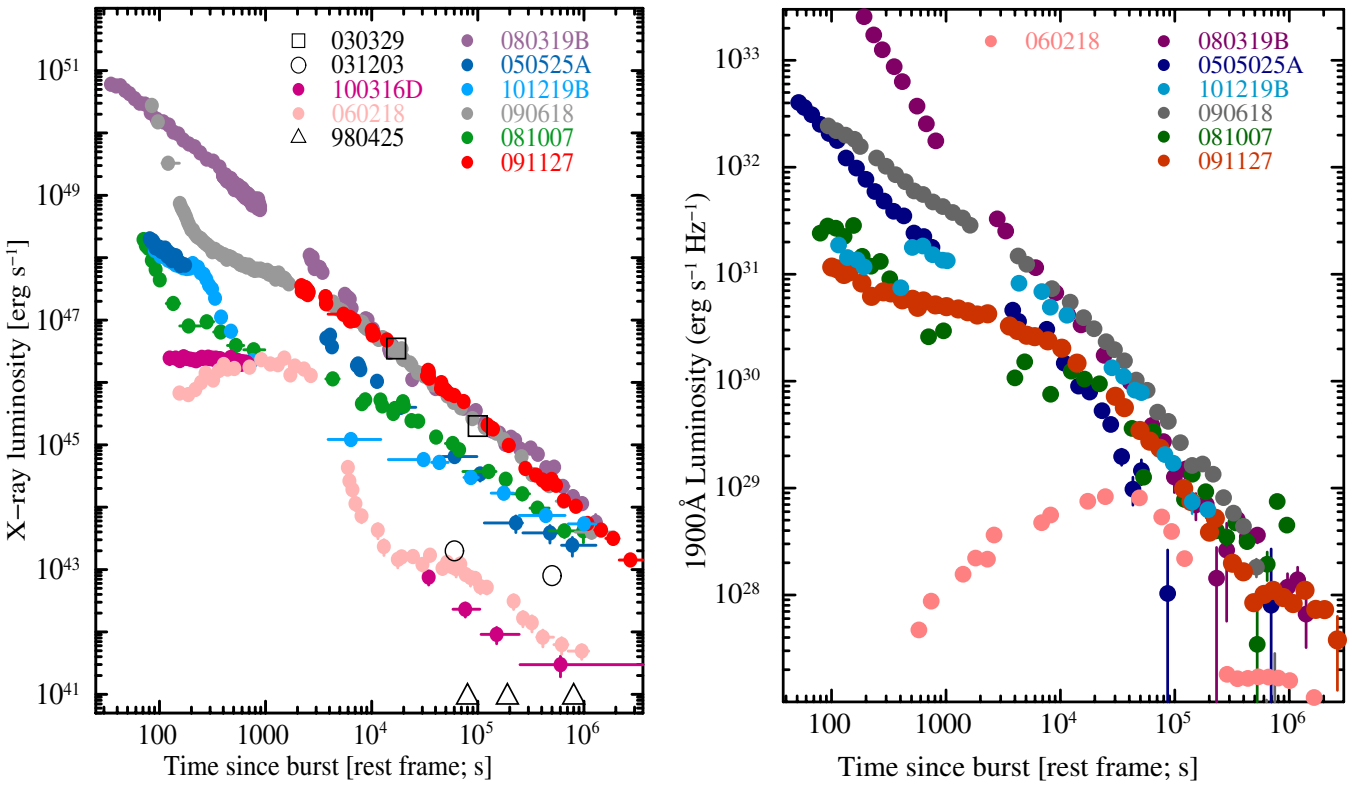

Figure 6. Left panel: rest-frame XRT afterglow light curves for *Swift* GRBs with an associated SN (filled circles). We also report the data for the three pre-*Swift* bursts with a spectroscopically confirmed SN (open symbols; Kaneko et al. 2007). Right panel: rest-frame UVOT afterglow light curves. Only GRBs with an UVOT detection are shown. Early-time LT/FTS data for GRB 091127 are also reported.

(A color version of this figure is available in the online journal.)

a blackbody (single or multi-temperature) yield a significant improvement in the fit statistics, although such a component is not inconsistent with the data.

The spectrum of the second peak (interval *b*) can be well described by a Band function. The inclusion of the LAT data yields a steeper high-energy spectral slope than the one derived from the GBM only fit, and the addition of a high-energy break is not required by the data. According to this model, the observed fluence during this interval is $(4.5 \pm 0.2) \times 10^{-6}$ erg cm^{-2} in the 8–1000 keV energy band, corresponding to an isotropic equivalent energy $E_{\gamma,\mathrm{iso}} = (4.3 \pm 0.3) \times 10^{51}$ erg in the 1–10,000 keV rest-frame energy band.

4.2. Afterglow Properties

In Figure 6, we compare the afterglow of GRB 091127 to the sample of *Swift* GRBs with bona fide SN associations (Hjorth & Bloom 2011). The observed XRT and UVOT light curves were corrected for redshift and absorption effects, and shifted to a common rest-frame energy band of 0.3–10 keV (XRT) and a rest-frame wavelength of 1900 Å (UVOT; Oates et al. 2009). From an afterglow perspective, GRB 091127 resembles the behavior of typical long GRBs, dominated by the bright emission from the external forward shock, rather than the unusual evolution of nearby GRBs. The isotropic X-ray luminosity at $t = 11$ hr is $L_{X,\mathrm{iso}} \sim 2 \times 10^{45}$ erg s^{-1}, very similar to GRB 030329, and a factor of $>10^3$ brighter than GRB 031203 and other GRBs/SNe. The UV/optical afterglows appear instead to decay more rapidly and to cluster at late times, but this could be the result of an observational bias, as the chance of discovering a SN is higher if the optical afterglow is faint.

If the afterglow emission of GRB 091127 is mainly synchrotron radiation from the external forward shock, its broadband behavior has to obey the fireball model closure relations (e.g., Zhang & Mészáros 2004). We found that the GRB afterglow is roughly consistent with a model of a narrow jet expanding into a homogeneous surrounding medium. Our results agree well with previous studies (Vergani et al. 2011; Filgas et al. 2011). The fireball model describes the emission from a population of accelerated electrons with energy distribution $n(\epsilon) \propto \epsilon^{-p}$. From the afterglow spectral properties we derive an electron index $p = 1.60^{+0.10}_{-0.02}$, which is at the lower end of the p distribution but not uncommon (Panaitescu & Kumar 2002). An achromatic break is detected at ~8 hr, after which the X-ray and optical light curves decay with a similar slope of ~1.6. This behavior is suggestive of an early jet-break. The presence of a jet-break at early times is also supported by our *Chandra* observations, which do not show evidence of a steepening in the X-ray light curve several months after the burst. We found that any possible late time jet-break is constrained to $t > 115$ d, which, for typical parameters, would imply an unusually large opening angle $\theta_j > 30°$. Instead, the two *Chandra* points hint at a shallower decline, as expected for example in the transition to the non-relativistic phase (Piro et al. 2001; Tiengo et al. 2004).

The SED analysis (Section 3.4) shows that optical and X-ray data belong to different branches of the synchrotron spectrum, since the cooling frequency ν_c lies between the two energy bands. The observed break at 30 ks is therefore not connected to spectral variations or changes in the ambient density. Figure 3 shows that at 6 ks the lowest optical flux produced by the X-ray source (with ν_c just below X-rays) would be only a factor $\lesssim$2 lower than measured, thus the reverse shock contribution

to the total optical flux (Kobayashi 2000) is negligible and optical and X-ray emission mainly arise from the same source (external forward shock). In this framework, the evolution of the cooling frequency is tied to the observed X-ray and optical decays by the following relation (Panaitescu et al. 2006):

$$-\frac{d\ln \nu_c}{d\ln t} = 2(\alpha_X - \alpha_{\rm opt}) = 0.94 \pm 0.11. \quad (1)$$

This is consistent with our spectral fits, which measure a cooling frequency that is rapidly moving downwards in energy as $\nu_c \propto t^{-1.5\pm0.5}$, as independently found in Filgas et al. (2011). For constant microphysical parameters, a decreasing ν_c suggests an interstellar medium (ISM) environment rather than a wind-like density profile, where the cooling frequency is expected to increase with time. In a uniform density medium, the cooling break evolves as $\nu_c \propto E^{-1/2}\epsilon_B^{-3/2}t^{-1/2}$ for a spherical expansion, and as $\nu_c \propto E^{-2/3}\epsilon_B^{-3/2}t^0$ in the jet spreading phase (Panaitescu & Kumar 2002, 2004). For constant microphysical parameters and no energy injection into the blast wave, the expected decay is shallower than the observed one. This shows that the simplest version of the fireball model cannot account for the overall afterglow behavior, and, as we will discuss in Section 5.2, some modifications (e.g., energy injection or evolving microphysical parameters) are required.

5. DISCUSSION

5.1. Origin of the High-energy Spectral Break

The most recent *Fermi* observations of GRBs suggested that the prompt γ-ray emission can be satisfactorily described by a smoothly broken power-law, the Band function, extending to the GeV energies, often accompanied by an additional non-thermal component modeled as a power-law (Guetta et al. 2011; Zhang et al. 2011). In this burst we found that a standard Band function, though providing an adequate description of the spectrum in the keV energy range, is in contrast with the simultaneous *Fermi*/LAT observations as it overpredicts the observed emission above 100 MeV (see Figure 5). The spectral fits presented in Tables 1 and 2 detect the presence of a spectral softening at ≈0.5–1 MeV in the time-integrated spectrum and during the first peak of emission. This disfavors spectral evolution as the origin of the observed feature.

A steepening of the high-energy spectral slope could be caused by several factors, such as absorption from the extragalactic background light (EBL), attenuation via pair production ($\gamma\gamma \rightarrow e^{\pm}$) or an intrinsic break in the energy distribution of the emitting electrons. Based on the low redshift of this burst ($z = 0.49$) and the low energy of the observed break, EBL absorption can be excluded (see, e.g., Finke et al. 2010). Below we consider in turn the other possibilities.

Optical depth effects. The lack of high-energy photons in bright bursts such as GRB 091127 could be an indication of a pair opacity break (Guetta et al. 2011), and therefore used to constrain the outflow Lorentz factor (Lithwick & Sari 2001). In order to be self-consistent, these calculations rely on the fundamental assumption that the observed sub-MeV spectrum extrapolates to GeV energies. Following this line of argument, we can set a first upper limit on the bulk Lorentz factor in GRB 091127 just by considering its non-detection by LAT. We use here the Band function parameters and impose $E_{\rm max} < 100$ MeV:

$$\Gamma_{\gamma\gamma} < 130\left[\left(\frac{E_{\rm max}}{100\ {\rm MeV}}\right) f_{100}\ t_v^{-1}\right]^{\frac{1}{2\beta+2}}, \quad (2)$$

where $\beta = 2.28$ is the high-energy spectral slope and $f_{100} \sim 0.1$ photons cm^{-2} s^{-1} keV^{-1} is the observed flux density at 100 keV, both derived from the spectral fit in Table 1. The variability timescale was set to $t_v \approx 0.3$ s, the minimum value observed in the γ-ray light curve. In deriving Equation (2) we approximated the spectral shape with a simple power-law, $f_\nu \propto \nu^{-\beta}$, which is valid when the energy of the target photons (in the observer's frame) is $E_t \gg E_{\rm pk} \sim 45$ keV. Given that $E_{\rm max} \sim 100$ MeV this is satisfied if $\Gamma_{\gamma\gamma} \gg 6$.

The upper limit derived in Equation (2) is based on the simple formulation given in Lithwick & Sari (2001), where spatial and temporal dependencies are averaged out. More realistic calculations taking into account the progressive buildup of the radiation field further decrease the above value by a factor of 2–3 (Hascoët et al. 2011), that is $\Gamma_{\gamma\gamma} \approx 50$. This is significantly lower than the values estimated for cosmological GRBs (Molinari et al. 2007; Liang et al. 2010), though similar to the Lorentz factor inferred for X-ray flares (Abdo et al. 2011). If we now take into account the observed steepening at $\lesssim$1 MeV as it originates from an increase in the optical depth, by setting $E_{\rm max} \simeq E_{\rm cut}$ we get $\Gamma \approx 2$. Such a low Lorentz factor, though atypical for classical GRBs, is not unprecedented (Soderberg et al. 2006). A weakly relativistic outflow could therefore account for the lack of high-energy photons and the observed soft spectrum, but not for the bright afterglow detected a few minutes after the burst.

An independent estimate of the bulk Lorentz factor can be derived from afterglow observations. The duration of the GRB being rather short, we consider the thin shell case (Kobayashi et al. 1999). Since the afterglow is already fading in our first observation we can assume that the onset happened at $t_{\rm pk} < 140\ (1+z)^{-1} \sim 100$ s, and set a lower limit to the outflow Lorentz factor Γ_0 (Piran 1999):

$$\Gamma_0 > 240\left(\frac{E_{\gamma,52}}{\eta_{0.2} n t_{\rm pk,2}^3}\right)^{1/8}, \quad (3)$$

where $E_\gamma = 10^{52}\ E_{\gamma,52}$ erg is the isotropic-equivalent energy, $\eta = 0.2\eta_{0.2}$ is the radiative efficiency and $n \sim 1$ cm^{-3} is the medium density (Bloom et al. 2003). By using the empirical relation suggested by Liang et al. (2010), we infer a similar high value of $\Gamma_0 \sim 200$.

The limits derived from the prompt and afterglow emission properties are inconsistent: the former suggest a mildly relativistic outflow ($\Gamma < 50$, or even $\Gamma \approx 2$), the latter a highly relativistic jet ($\Gamma \gg 100$). A possibility that would reconcile the two sets of limits is that the first spectrally softer pulse, during which we detect the significant presence of a spectral break, is instead the GRB precursor originating at $R \approx 2\Gamma^2 c t_v \approx 10^{11}$ cm, e.g., from the jet cocoon emerging from the progenitor star (Lazzati & Begelman 2005). A different physical origin could also explain the different lags between the two main γ-ray events and the unusual lag evolution: while spectral lags in GRB pulses generally tend to increase with time (Hakkila et al. 2008), it has been found that precursors have larger lags than the following γ-ray emission (Page et al. 2007). However, on theoretical grounds, precursors are expected to carry only a small fraction of the total energy release (Morsony et al. 2007), while the first peak encloses 50% of the observed γ-ray fluence.

Similarly, the analysis of Burlon et al. (2008) found that the observed precursors in long GRBs have energetics comparable to the main prompt emission, and it remains unclear whether they are distinct from the prompt emission phase, or they are part of the same phenomenon.

We therefore are led to consider that our assumption of a pair opacity break is not valid, that is: (1) the inconsistency between Equations (2) and (3) implies that the Band-type spectrum does not extend to GeV energies, but a spectral break (not related to optical depth effects) below 100 MeV is required by the data; (2) we identify this break with the steepening at ≈0.7 MeV, which is therefore an intrinsic feature of the GRB spectrum.

Breaks in GRB spectra. We discuss here the standard scenario, in which internal shocks within the expanding outflow accelerate the ambient electrons to relativistic energies with a power-law distribution $n(\epsilon) \propto \epsilon^{-p}$. The GRB prompt emission originates as synchrotron radiation from the shock-accelerated electrons. The small ratio between the GeV and keV fluences of this burst, $\mathcal{F}_{\rm GeV}/\mathcal{F}_{\rm keV} \lesssim 0.01$, disfavors Synchrotron Self-Compton as the main radiation mechanism.

The observed properties of the first γ-ray peak, are roughly in agreement with a synchrotron spectrum. The high-energy slope $\beta \sim -2$ suggests that for $E > 50$ keV we are already above the injection frequency ν_m. The low-energy slope $\alpha \sim -0.4$ is not consistent with the value of -1.5 for the fast cooling regime, but can be still accounted for if the effects of adiabatic and radiative cooling are comparable (marginally fast cooling; Daigne et al. 2011). In the extreme case $\Gamma_c/\Gamma_m \sim 10$, synthetic spectra resemble the observed spectral shape: a hard low-energy tail followed by a smooth, flat transition ($\nu_m < \nu < \nu_c$) to the final $F_\nu \propto \nu^{-p/2}$ decay. The observed steepening at ≈0.7 MeV from $\beta \sim -2$ to < -2.6 corresponds to this transition, and implies $p \gtrsim 3.2$. However, when the slow cooling contribution is dominant, the radiative efficiency decreases markedly (Daigne et al. 2011), and it is hard to account for the high luminosity and variability of the prompt emission. If we consider the more efficient case of $\Gamma_c/\Gamma_m \sim 1$, then the spectral break has to be ascribed to a different mechanism.

A spectral cutoff is expected at $\nu(\gamma_M)$, where γ_M is the maximum Lorentz factor of the shocked electrons. Such a break occurs at energies $\gtrsim$200 MeV (Bošnjak et al. 2009), and it is unlikely at the origin of the MeV break. An alternative explanation is an intrinsic curvature in the energy distribution of the radiating electrons (Massaro et al. 2010), arising if the higher energy electrons are accelerated less efficiently than those with lower energy.

5.2. Jet Collimation and Energetics

From our broadband spectral fits of the prompt emission we derived an isotropic equivalent energy $E_{\gamma,\rm iso} = (1.1 \pm 0.2)\times10^{52}$ erg, which is in the typical range of long GRBs (Bloom et al. 2003). The afterglow properties show evidence of a tightly collimated outflow, indicating that the true energy release is significantly lower. The achromatic nature of the break at $t_{\rm bk} \sim 30$ ks and the subsequent afterglow fast decay are typical signatures of a jet-break, and we first consider this hypothesis. In this scenario the jet opening angle θ_j is

$$\theta_j = 4.2 \left(\frac{E_{\rm iso,52}}{\eta_{0.2} n}\right)^{-1/8} \left(\frac{t_{\rm bk}}{8\,{\rm hr}}\right)^{3/8} {\rm deg}, \quad (4)$$

and the collimation-corrected energy is $E_{\gamma,j} = (3.0 \pm 0.8)\times10^{49}$ erg. This is an order of magnitude lower than the canonical value of $\sim 5 \times 10^{50}$ erg quoted for long GRBs (e.g., Cenko et al. 2010). In this scenario, the burst is consistent with the Ghirlanda relation (Vergani et al. 2011). However, as noted in Section 4.2, this simple fireball scenario fails to reproduce two main features: (1) the rapid temporal evolution of the cooling frequency; (2) the observed pre-break flux decay rates ($\alpha_X = 1.03 \pm 0.04$, $\alpha_{\rm opt} = 0.56 \pm 0.04$), which are not compatible with the model expectations ($\alpha_{\nu>\nu_c} \sim 0.7$, $\alpha_{\nu_c>\nu>\nu_m} \sim 0.45$ for a spreading jet; $\alpha_{\nu>\nu_c} = \alpha_{\nu_c>\nu>\nu_m} \sim 0.8$ for a non-spreading jet; Panaitescu & Kumar 2004). In order to reconcile the observed afterglow behavior with the theoretical expectations, one needs to invoke either a continual energy injection and/or evolving microphysical parameters. The former scenario would require an extreme injection episode, the jet energy increasing by a factor of 100 in the first 8 hr. Furthermore, there is no apparent reason for the injection to end at the time of the jet-break, leading to an even larger shock energy carried by the slower ejecta. The alternative possibility of a growing magnetic energy fraction ϵ_B is discussed by Filgas et al. (2011).

We found instead that a narrow confined jet, whose boundary is visible from the first afterglow measurement (i.e., $\Gamma < \theta_j^{-1}$), and a prolonged energy injection, lasting until ∼30 ks, provide a consistent description of the afterglow temporal and spectral properties and ease the energetic burden without requiring any variation of the shock microphysical parameters. For an ISM-like circumburst medium (Section 4.2), the flux decay indices are given by (Panaitescu & Kumar 2004)

$$\alpha_o = \frac{3}{4}p - \frac{p+4}{4}e, \quad (5)$$

$$\alpha_X = \frac{3p+1}{4} - \frac{p+3}{4}e, \quad (6)$$

where e is the power-law evolution of the forward-shock energy $E \propto t^e$. The above set of equations overconstrain the e parameter, thus providing a consistency check of the solution. By substituting in Equations (5) and (6) the observed pre-break temporal slopes and the value of $p \sim 1.6$ from the broadband spectral fit, we derive $e = 0.48 \pm 0.06$ and $e = 0.39 \pm 0.06$, respectively. Departures of the energy injection from a pure power-law can explain the optical plateau at $t < 5$ ks, while the cessation of energy injection at ≈30 ks yields the observed achromatic break. According to this model, by imposing $t_{\rm bk} < 140$ s in our Equation (4) we derive $\theta_j \lesssim 0.6\,(n/1\ {\rm cm}^{-3})^{1/8}$ deg, and $E_\gamma \lesssim 6\times10^{47}\,(n/1\ {\rm cm}^{-3})^{1/4}$ erg. By using $e \sim 0.45$, the blast wave kinetic energy can be constrained to $E_{\rm K} \lesssim 3\times10^{50}$ erg, most of which comes from the slower ejecta that are gradually replenishing the forward-shock energy.

From our analysis the following features clearly emerge: GRB 091127 is characterized by a highly collimated outflow ($\theta_j \lesssim 4^\circ$), a low prompt γ-ray energy ($E_\gamma < 3 \times 10^{49}$ erg), and a total relativistic energy yield of $E_{\rm rel} \lesssim 3 \times 10^{50}$ erg, at the lower end of the long GRBs distribution. In Figure 7, we compare the burst energetics with the sample of long GRBs. Independently from the afterglow model adopted (I, narrow jet + energy injection: star; II, evolving ϵ_B: diamond), the burst location in the lower left corner shows that GRB 091127 more closely resembles the class of X-ray Flashes (XRFs) and GRBs/SNe rather than typical GRBs. This is also consistent with its rather soft spectrum and unusual lags.

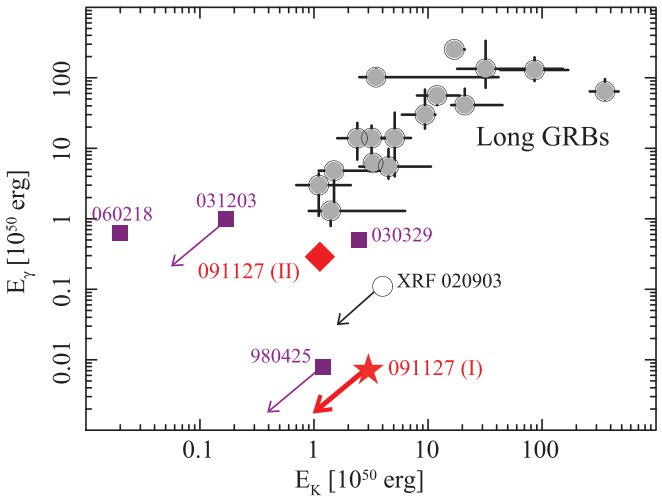

Figure 7. Prompt emission energy release, E_γ, vs. afterglow kinetic energy, E_K. For GRB 091127 both the scenarios discussed in the text are shown: (I) narrow jet + prolonged energy injection; (II) evolving ϵ_B. We report data for standard long GRBs (filled circles), XRFs (open circles), and bursts with a spectroscopic SN (squares). Values are corrected for collimation effects. References: Panaitescu & Kumar 2002; Bloom et al. 2003; Soderberg et al. 2004; Cenko et al. 2010.

(A color version of this figure is available in the online journal.)

6. SUMMARY AND CONCLUSION

We presented a broadband analysis of the prompt and afterglow emission of GRB 091127, securely associated with SN2009nz. Two main features emerged from our study of the prompt emission: (1) the burst is characterized by small, negligible spectral lags and (2) the high-energy (>100 MeV) emission is significantly suppressed. The GRB has a long duration ($T_{90} \sim 7$ s), and a relatively soft spectrum ($E_{\rm pk} \approx 45$ keV). However, having negligible spectral lags and only a moderate luminosity, the burst does not fit the lag–luminosity relation followed by cosmological long GRBs, but lies in the region of short-duration bursts. While the association with SN2009nz leaves no doubts about the origin of the GRB progenitor, the atypical lag behavior adds additional uncertainty in the classification of GRBs based solely on their high-energy properties. It also links GRB 091127 to nearby sub-energetic bursts, such as GRB 980425, which are also outliers of the lag-luminosity relation.

By modeling the GRB prompt emission with the standard Band function, we found that such a model significantly overpredicts the observed flux at higher (>100 MeV) energies. Consistently, our spectral fits show evidence of a spectral curvature at energies $\lesssim$1 MeV. If due to opacity effects, the suppression of high-energy emission would suggest a low outflow Lorentz factor ($\Gamma < 50$, or even $\Gamma \approx 2$), as measured in nearby sub-energetic GRBs. However, this interpretation is not consistent with our early-time detection of a bright fading afterglow, which suggests $\Gamma \gg 100$. We therefore conclude that the high-energy break is an intrinsic property of the GRB spectrum.

The multi-wavelength afterglow emission is characterized by an achromatic break at ~8 hr after the burst, and by a rapidly decaying cooling frequency, $\nu_c \propto t^{-1.5\pm0.5}$. We considered two scenarios to interpret these features within the standard fireball model. The former interprets the achromatic break as a jet-break, from which we derive a jet opening angle $\theta_j \approx 4^\circ$, and a collimation-corrected energy $E_\gamma \approx 3 \times 10^{49}$ erg. This model needs to let the microphysical parameters vary with time in order to reproduce the observed temporal decays and the rapidly decreasing ν_c. The latter scenario instead interprets the achromatic break as the end of a prolonged energy injection episode, the jet-break happening before the start of our observations ($t < 140$ s). According to this model, we derive a jet opening angle $\theta_j \lesssim 0.6$ deg, and a collimation-corrected energy $E_\gamma \lesssim 6 \times 10^{47}$ erg. This GRB therefore presents hybrid properties: a high-luminosity γ-ray emission powered by narrowly collimated and highly relativistic outflow as typical of long GRBs; its low-energy output, rather soft spectrum and location in the lag–luminosity plan more closely resembles the class of XRFs and GRBs/SNe.

We thank T. Ukwatta, R. Starling, and R. Filgas for useful discussions and information. E.T. was supported by an appointment to the NASA Postdoctoral Program at the Goddard Space Flight Center, administered by Oak Ridge Associated Universities through a contract with NASA. This work made use of data supplied by the UK Swift Science Data Centre at the University of Leicester. The *Konus–Wind* experiment is supported by a Russian Space Agency contract and RFBR Grant 11-02-12082-ofi_m.

The *Fermi* LAT Collaboration acknowledges generous ongoing support from a number of agencies and institutes that have supported both the development and the operation of the LAT as well as scientific data analysis. These include the National Aeronautics and Space Administration and the Department of Energy in the United States, the Commissariat à l'Energie Atomique and the Centre National de la Recherche Scientifique/Institut National de Physique Nucléaire et de Physique des Particules in France, the Agenzia Spaziale Italiana and the Istituto Nazionale di Fisica Nucleare in Italy, the Ministry of Education, Culture, Sports, Science and Technology (MEXT), High Energy Accelerator Research Organization (KEK) and Japan Aerospace Exploration Agency (JAXA) in Japan, and the K. A. Wallenberg Foundation, the Swedish Research Council and the Swedish National Space Board in Sweden. Additional support for science analysis during the operations phase is gratefully acknowledged from the Istituto Nazionale di Astrofisica in Italy and the Centre National d'Études Spatiales in France.

REFERENCES

Abdo, A. A., Ackermann, M., Ajello, M., et al. 2011, ApJ, 734, L27
Abdo, A. A., Ackermann, M., Asano, K., et al. 2009, ApJ, 707, 580
Amati, L., Della Valle, M., Frontera, F., et al. 2007, A&A, 463, 913
Arnaud, K., Smith, R., & Siemiginowska, A. 2011, Handbook of X-ray Astronomy (Cambridge: Cambridge Univ. Press), 7
Atwood, W. B., Abdo, A. A., Ackermann, M., et al. 2009, ApJ, 697, 1071
Band, D., Matteson, J., Ford, L., et al. 1993, ApJ, 413, 281
Barthelmy, S. D., Barbier, L. M., Cummings, J. R., et al. 2005, Space Sci. Rev., 120, 143
Berger, E., Chornock, R., Holmes, T. R., et al. 2011, ApJ, 743, 204
Berger, E., Kulkarni, S. R., Pooley, G., et al. 2003, Nature, 426, 154
Bloom, J. S., Frail, D. A., & Kulkarni, S. R. 2003, ApJ, 594, 674
Bloom, J. S., Kulkarni, S. R., Djorgovski, S. G., et al. 1999, Nature, 401, 453
Bošnjak, Ž., Daigne, F., & Dubus, G. 2009, A&A, 498, 677
Breeveld, A. A., Curran, P. A., Hoversten, E. A., et al. 2010, MNRAS, 406, 1687
Burlon, D., Ghirlanda, G., Ghisellini, G., et al. 2008, ApJ, 685, L19
Burrows, D. N., Hill, J. E., Nousek, J. A., et al. 2005, Space Sci. Rev., 120, 165
Cash, W. 1979, ApJ, 228, 939
Cenko, S. B., Frail, D. A., Harrison, F. A., et al. 2010, ApJ, 711, 641
Chapman, R., Tanvir, N. R., Priddey, R. S., & Levan, A. J. 2007, MNRAS, 382, L21
Cobb, B. E., Bloom, J. S., Perley, D. A., et al. 2010, ApJ, 718, L150
Daigne, F., Bošnjak, Ž., & Dubus, G. 2011, A&A, 526, A110
Della Valle, M., Malesani, D., Bloom, J. S., et al. 2006, ApJ, 642, L103
Esin, A. A., & Blandford, R. 2000, ApJ, 534, L151

Evans, P. A., Beardmore, A. P., Page, K. L., et al. 2007, A&A, 469, 379
Filgas, R., Greiner, J., Schady, P., et al. 2011, A&A, 535, A57
Finke, J. D., Razzaque, S., & Dermer, C. D. 2010, ApJ, 712, 238
Galama, T. J., Vreeswijk, P. M., van Paradijs, J., et al. 1998, Nature, 395, 670
Gehrels, N., Chincarini, G., Giommi, P., et al. 2004, ApJ, 611, 1005
Gehrels, N., Norris, J. P., Barthelmy, S. D., et al. 2006, Nature, 444, 1044
Ghirlanda, G., Celotti, A., & Ghisellini, G. 2003, A&A, 406, 879
Guetta, D., Pian, E., & Waxman, E. 2011, A&A, 525, A53
Guidorzi, C., Monfardini, A., Gomboc, A., et al. 2006, PASP, 118, 288
Haislip, J., Reichart, D., Ivarsen, K., et al. 2009, GRB Coordinates Network, 10219
Hakkila, J., Giblin, T. W., Norris, J. P., Fragile, P. C., & Bonnell, J. T. 2008, ApJ, 677, L81
Hascoët, R., Daigne, F., Mochkovitch, R., & Vennin, V. 2011, arXiv:1110.6313
Hjorth, J., & Bloom, J. S. 2011, Gamma-Ray Bursts, ed. C. Kouveliotou, R. A. M. J. Wijers, & S. E. Woosley (Cambridge: Cambridge Univ. Press)
Jordi, K., Grebel, E. K., & Ammon, K. 2006, A&A, 460, 339
Kalberla, P. M. W., Burton, W. B., Hartmann, D., et al. 2005, A&A, 440, 775
Kaneko, Y., Ramirez-Ruiz, E., Granot, J., et al. 2007, ApJ, 654, 385
Kobayashi, S. 2000, ApJ, 545, 807
Kobayashi, S., Piran, T., & Sari, R. 1999, ApJ, 513, 669
Lampton, M., Margon, B., & Bowyer, S. 1976, ApJ, 208, 177
Landolt, A. U. 1992, AJ, 104, 340
Lazzati, D., & Begelman, M. C. 2005, ApJ, 629, 903
Liang, E., Yi, S., Zhang, J., et al. 2010, ApJ, 725, 2209
Liang, E., Zhang, B., Virgili, F., & Dai, Z. G. 2007, ApJ, 662, 1111
Lithwick, Y., & Sari, R. 2001, ApJ, 555, 540
Massaro, F., Grindlay, J. E., & Paggi, A. 2010, ApJ, 714, L299
McBreen, S., Foley, S., Watson, D., et al. 2008, ApJ, 677, L85
Molinari, E., Vergani, S. D., Malesani, D., et al. 2007, A&A, 469, L13
Morsony, B. J., Lazzati, D., & Begelman, M. C. 2007, ApJ, 665, 569
Nava, L., Salvaterra, R., Ghirlanda, G., et al. 2012, MNRAS, 421, 1256
Norris, J. P. 2002, ApJ, 579, 386
Norris, J. P., & Bonnell, J. T. 2006, ApJ, 643, 266
Norris, J. P., Bonnell, J. T., Kazanas, D., et al. 2005, ApJ, 627, 324
Oates, S. R., Page, M. J., Schady, P., et al. 2009, MNRAS, 395, 490
Page, K. L., Willingale, R., Bissaldi, E., et al. 2009, MNRAS, 400, 134
Page, K. L., Willingale, R., Osborne, J. P., et al. 2007, ApJ, 663, 1125
Panaitescu, A., & Kumar, P. 2002, ApJ, 571, 779
Panaitescu, A., & Kumar, P. 2004, MNRAS, 350, 213
Panaitescu, A., Mészáros, P., Burrows, D., et al. 2006, MNRAS, 369, 2059
Pei, Y. C. 1992, ApJ, 395, 130
Pian, E., Mazzali, P. A., Masetti, N., et al. 2006, Nature, 442, 1011
Piran, T. 1999, Phys. Rep., 314, 575
Piro, L., Garmire, G., Garcia, M. R., et al. 2001, ApJ, 558, 442
Roming, P. W. A., Kennedy, T. E., Mason, K. O., et al. 2005, Space Sci. Rev., 120, 95
Ryde, F., Axelsson, M., Zhang, B. B., et al. 2010, ApJ, 709, L172
Sakamoto, T., Pal'Shin, V., Yamaoka, K., et al. 2011, PASJ, 63, 215
Smith, R. J., Kobayashi, S., Guidorzi, C., & Mundell, C. G. 2009, GRB Coordinates Network, 10192, 1
Soderberg, A. M., Kulkarni, S. R., Berger, E., et al. 2004, Nature, 430, 648
Soderberg, A. M., Kulkarni, S. R., Nakar, E., et al. 2006, Nature, 442, 1014
Sparre, M., Sollerman, J., Fynbo, J. P. U., et al. 2011, ApJ, 735, L24
Starling, R. L. C., Wiersema, K., Levan, A. J., et al. 2011, MNRAS, 411, 2792
Starling, R. L. C., Wijers, R. A. M. J., Wiersema, K., et al. 2007, ApJ, 661, 787
Tanvir, N. R., Rol, E., Levan, A. J., et al. 2010, ApJ, 725, 625
Tiengo, A., Mereghetti, S., Ghisellini, G., Tavecchio, F., & Ghirlanda, G. 2004, A&A, 423, 861
Troja, E., Barthelmy, S. D., Baumgartner, W. H., et al. 2009, GRB Coordinates Network, 10191, 1
Ukwatta, T. N., Stamatikos, M., Dhuga, K. S., et al. 2010, ApJ, 711, 1073
Vergani, S. D., Flores, H., Covino, S., et al. 2011, A&A, 535, A127
Virgili, F. J., Zhang, B., O'Brien, P., & Troja, E. 2011, ApJ, 727, 109
Waxman, E., & Draine, B. T. 2000, ApJ, 537, 796
Woosley, S. E., & Bloom, J. S. 2006, ARA&A, 44, 507
Zeh, A., Klose, S., & Hartmann, D. H. 2004, ApJ, 609, 952
Zhang, B., & Mészáros, P. 2004, Int. J. Mod. Phys. A, 19, 2385
Zhang, B., Zhang, B., Liang, E., et al. 2011, ApJ, 730, 141
Zhang, B., Zhang, B.-B., Virgili, F. J., et al. 2009, ApJ, 703, 1696